

Atomic Layer Deposition of Platinum Nanoparticles on Titanium Oxide and Tungsten Oxide Using Platinum(II) Hexafluoroacetylacetonate and Formalin as the Reactants

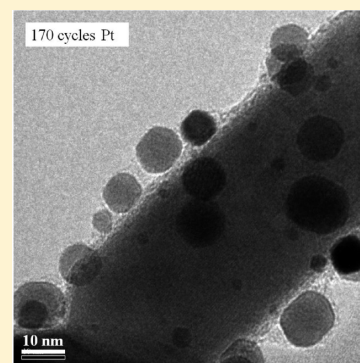
Virginia R. Anderson,[†] Noemi Leick,[§] Joel W. Clancey,[†] Katherine E. Hurst,^{||} Kim M. Jones,^{||} Anne C. Dillon,^{||} and Steven M. George^{*,†,‡}

[†]Department of Chemistry and Biochemistry and [‡]Department of Mechanical Engineering, University of Colorado, Boulder, Colorado 80309, United States

[§]Technische Universiteit Eindhoven, P.O. Box 513, 5600 MB Eindhoven, The Netherlands

^{||}National Renewable Energy Laboratory, 1617 Cole Boulevard, Golden, Colorado 80401, United States

ABSTRACT: Pt nanoparticles were grown on titanium oxide and tungsten oxide at 200 °C by Pt atomic layer deposition (ALD) using platinum(II) hexafluoroacetylacetonate [Pt(hfac)₂] and formalin as the reactants. The Pt ALD surface chemistry and Pt nanoparticles were examined using in situ Fourier transform infrared (FTIR) vibrational spectroscopy and ex situ transmission electron microscopy (TEM). The FTIR spectra identified the surface species after the Pt(hfac)₂ and formalin exposures on TiO₂. An infrared feature at ~2100 cm⁻¹ in the FTIR spectrum after Pt(hfac)₂ and formalin exposures on TiO₂ was consistent with CO on Pt, revealing that Pt(hfac)₂ and formalin exposures led to the formation of Pt nanoparticles. The FTIR spectrum of Pt(hfac)₂ on TiO₂ was very similar to the FTIR spectrum of hexafluoroacetylacetonate (hfacH) on TiO₂. The FTIR spectra also revealed that hfacH blocked the adsorption of Pt(hfac)₂ on TiO₂. The coverage of the Pt nanoparticles could be reduced by preadsorbing hfacH on TiO₂ prior to Pt(hfac)₂ adsorption. Time-dependent FTIR spectra showed that the coverage of hfacH and its adsorption products were reduced versus time following hfacH exposure. Pt ALD on WO_x at 200 °C led to the growth of Pt nanoparticles that were fairly similar to the Pt nanoparticles from Pt ALD on TiO₂. The TEM images revealed that the size of the Pt nanoparticles on WO_x could be adjusted by varying the number of Pt ALD cycles. Because of site-blocking by the hfac ligands, the Pt(hfac)₂ and formalin reactants required many more ALD cycles for nucleation and growth compared with other Pt ALD surface chemistries.



1. INTRODUCTION

Platinum is one of the most important catalysts in heterogeneous catalysis. Platinum is also extremely resistant to oxidation¹ and is a common electrode material in oxygen-containing and aqueous environments. Platinum is especially important as a catalyst for the oxygen reduction reaction (ORR) in polymer electrolyte membrane (PEM) fuel cells.² Unfortunately, Pt is a precious metal and its high cost requires that Pt be used very efficiently. Approximately ~80 g of Pt catalyst were required for 75 kW PEM automotive fuel cells in 2005.² Although the Pt requirements have decreased in recent years, there is still an economic need to reduce the amount of Pt to reduce the fuel cell cost. One possibility is that Pt can be deposited with greater control using atomic layer deposition (ALD) techniques.³

Pt ALD was initially reported using (methylcyclopentadienyl)trimethylplatinum (MeCpPtMe₃) and O₂ as the reactants.⁴ The mechanism of this reaction is based on combustion chemistry where the oxygen burns the organic ligands from the Pt precursor.^{5,6} The nucleation of Pt ALD can be greatly facilitated using MeCpPtMe₃ and an O₂ plasma as the reactants.^{7,8} Pt ALD can also be achieved using

Pt(acac)₂ and ozone.⁹ In addition to combustion chemistry, Pt ALD can be defined using Pt precursors together with reducing agents. One example of this reduction chemistry for Pt ALD is the use of MeCpPtMe₃ and H₂ plasma as the reactants.¹⁰ Other reducing agents can also be employed, such as formalin. Pt ALD using platinum(II) hexafluoroacetylacetonate [Pt(hfac)₂] and formalin should be similar to Pd ALD using Pd(hfac)₂ and formalin.^{11–13}

In contrast to ideal growth of ultrathin and conformal films using ALD,³ Pt ALD leads to the deposition of nanoparticles during initial film growth. Pt nanoparticles are observed during Pt ALD on carbon,^{14,15} carbon nanotube/graphene,^{15,16} TiO₂,^{17–20} SrTiO₃,^{18,21–24} ZnO,²⁵ WC,²⁶ Al₂O₃,^{18,27,28} SiO₂,^{27,29} and various sputtered metal films.³⁰ The appearance of Pt nanoparticles is linked to several causes. One factor is the lack of appropriate surface functional groups on the underlying substrate for the reaction with Pt ALD reactants.³¹ Another issue is the poisoning of the initial substrate by the ligands from

Received: December 22, 2013

Revised: March 30, 2014

Published: April 3, 2014

the Pt ALD reactants.^{12,13} In addition, perhaps the most important reason is the high surface energy of ~ 2.5 J/m² for platinum,³² which leads to the formation of Pt nanoparticles to minimize the Pt surface area to lower the surface energy.^{10,33}

In this work, Pt ALD was examined on titanium oxide and tungsten oxide surfaces. TiO₂ is an important metal oxide substrate for Pt in supported metal catalysis and photocatalysis.^{17–20} Pt–TiO₂ and Pt–WO₃ are also used as electrocatalysts in fuel cells because of their high activity, stability, and resistance to CO poisoning.^{34–37} The surface chemistry during the initial nucleation of Pt ALD on TiO₂ was explored using in situ FTIR vibrational spectroscopy studies. The growth of the Pt nanoparticles on titanium oxide and tungsten oxide was monitored using ex situ TEM investigations.

The goal of this work was to develop methods to control both the coverage and size of the Pt nanoparticles. The studies focused on Pt ALD using Pt(hfac)₂ and formalin as the reactants. Previous studies have observed that Pd ALD using palladium(II) hexafluoroacetylacetonate [Pd(hfac)₂] and formalin as the reactants leads to the formation of Pd nanoparticles on Al₂O₃ and TiO₂ substrates.^{11–13,38–41} Previous work on Pd ALD also showed that the hfac ligand was effective at blocking Pd(hfac)₂ reactant adsorption during Pd ALD.^{12,13} This site-blocking by the hfac ligand may provide a method to control the Pt nanoparticle coverage.

2. EXPERIMENTAL SECTION

The Pt ALD was performed in a vacuum reactor equipped for in situ FTIR analysis. This reactor has been previously described in detail.⁴² Briefly, the vacuum reactor was a warm wall viscous flow reactor. The walls of the reactor were maintained at ~ 130 °C. The reactor was constantly pumped with a mechanical pump (Alcatel 2010 C1). Using two mass flow controllers (URS-40), the N₂ gas in viscous flow was maintained at 1.25 Torr using a N₂ flow rate of 200 sccm. A capacitance manometer (MKS) monitored the N₂ viscous flow gas leaving the reactor. The N₂ flow gas was UHP grade (Airgas).

The precursors for the platinum growth were Pt(hfac)₂ (98% pure from Strem Chemicals Inc.) and formalin (37% formaldehyde and 10% methanol in water from Sigma-Aldrich). Both reactants were transferred to dosing vessels and degassed before experiments. To ensure appreciable vapor pressure, Pt(hfac)₂ was heated to 80 °C during the experiments. Formalin was maintained at room temperature.

The in situ FTIR experiments were performed using transmission FTIR through TiO₂ powder samples.⁴² Powder samples increase the sample surface area and improve the FTIR signal-to-noise compared with flat samples.^{43,44} The powders were pressed into a sample grid that could be resistively heated to high temperatures. The sample grid was made using a tungsten mesh with 100 lines per inch (Tech-Etch). The TiO₂ powders were mechanically pressed into this tungsten mesh. The tungsten oxide powders were also coated using the tungsten mesh.

The titanium dioxide nanopowder was crystalline with $\sim 80\%$ anatase and $\sim 20\%$ rutile (Nanophase Technologies Corp.). The tungsten oxide nanopowder was obtained from the National Renewable Energy Laboratory. The WO_x nanorods were grown using hotwire chemical vapor deposition in an argon and oxygen atmosphere.⁴⁵ The tungsten oxide had multiple oxidation states, including W, WO, and WO₃. The γ and monoclinic phases of tungsten oxide were present as

determined by X-ray diffraction. Thermogravimetric analysis indicated that the bulk oxidation state of the tungsten oxide was WO_{1.9}. Therefore, the tungsten oxide samples used for this work are designated as WO_x.

The TiO₂ and WO_x powder samples were pressed into the tungsten mesh and loaded into the reactor. The samples were purged with gaseous nitrogen for at least 1 h and then cleaned by annealing in vacuum to high temperature to remove carbon impurities. The TiO₂ powders were heated to 500 °C for 3–5 min. The WO_x nanorods were heated to 350 °C for 3–5 min. The tungsten mesh could reach temperatures over 650 °C. A temperature controller (Love Controls 16A) was used to control the temperature. A type K thermocouple was used to measure the temperature. The resistive heating current was supplied by a dc power supply (Hewlett-Packard 6268B).

The FTIR spectrometer was a Nicolet model Magna IR 560. CsI windows on the reactor allowed the infrared light to pass through the powder samples. The CsI windows were protected by gate valves during the reactant exposures. The infrared detector was a mercury cadmium telluride (MCT-B) detector. This MCT-B detector was cooled to 77 K with liquid nitrogen prior to use. The TiO₂ powder samples were sufficiently transparent for transmission FTIR studies. In contrast, the WO_x powders absorbed the infrared radiation because of their electrical conductivity.

X-ray photoelectron spectroscopy (XPS) was used to confirm that the Pt nanoparticles on the WO_x nanorods were metallic. The XPS analysis was performed using a PHI 5600 X-ray photoelectron spectrometer using a monochromatic Al K α source. The XPS depth-profiling to remove the surface carbon was conducted using argon sputtering. Transmission electron microscopy (TEM) was conducted at the National Renewable Energy Laboratory. The TEM was performed using an FEI Tecnai ST 30 TEM instrument with standard bright field electron diffraction contrast imaging operating at 200 kV.

3. RESULTS AND DISCUSSION

Parts a and b of Figure 1 show FTIR spectra from 2200 to 900 cm⁻¹ after the adsorption of hexafluoroacetylacetone (hfacH)

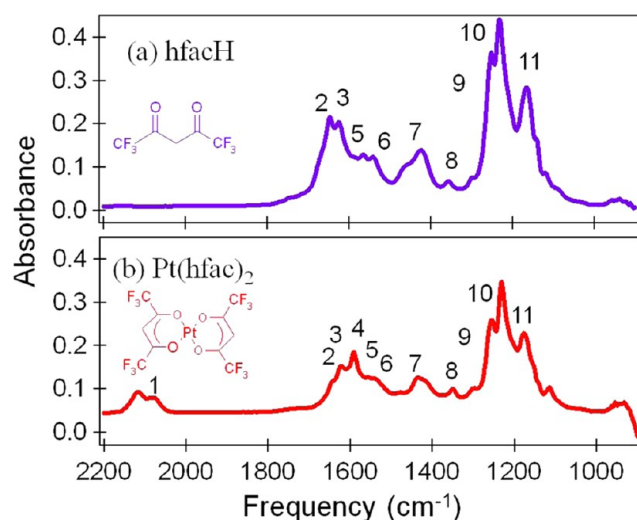


Figure 1. FTIR spectra after adsorption on TiO₂ powders at 200 °C. (a) Adsorption of hexafluoroacetylacetone (hfacH). (b) Adsorption of Pt(hfac)₂. The FTIR spectra are referenced to the initial TiO₂ powders. The peak assignments are given in Table 1.

and Pt(hfac)₂, respectively, to near saturation coverages on TiO₂ powders at 200 °C. These FTIR spectra are referenced to the initial TiO₂ powder. The similarities and differences of these two spectra are useful to identify the vibrational absorbances for hfacH and Pt(hfac)₂ on TiO₂ powders. The spectra are similar because both adsorbates share the same hfac group. The spectra are different because the Pt in the Pt(hfac)₂ leads to a distinct absorbance feature in the carbonyl region at 1590 cm⁻¹. This absorbance feature is assigned to Pt on the basis of the previous infrared spectroscopy studies of Pt(hfac)₂ and Pd(hfac)₂ on copper surfaces.^{46,47} Another distinct absorbance feature for Pt(hfac)₂ is the absorbance at ~2100 cm⁻¹ associated with CO on Pt nanoparticles.^{48–51} CO adsorbed on either anatase or rutile TiO₂ displays absorbance features at higher frequencies.^{52,53} The CO may be derived from residual CO gas in the reactor or decomposition of the hfac ligand.

All the vibrational assignments are given in Table 1. Many of the vibrational absorbance features correspond with intact

Table 1. Vibrational Mode Assignments after Pt(hfac)₂ and Formalin Exposures on TiO₂

mode no.	vibration	frequency (cm ⁻¹)	ref
1	CO on Pt/TiO ₂	~2100	48–51
2	C=C stretch	1640	54
3	C=O stretch	1625	54
4	Pt C=O + C–H bend	1590	46, 55
5	C=O stretch + C–H bend	1550	46, 55
6	C=C stretch	1530	55
7	C–H bend + C=C stretch	1440	54
8	C–C stretch + C–F stretch	1360	54, 56
9	CF ₃ stretch	1250	54, 56
10	CF ₃ stretch	1230	54, 56
11	C–H bend	1180	54, 56
12	C–H stretch	2942	59
13	C–H stretch	2837	59
14	COO stretch of formate	1550	59, 64, 65
15	COO stretch of formate	1370	59, 64, 65
16	C–O stretch	1026	59

HfacH or hfac ligand on the surface. The carbonyl C=O stretching vibrations are observed at 1640 and 1625 cm⁻¹.⁵⁴ A C=O stretching + CH bending combination band is also monitored at 1550 cm⁻¹.⁴⁶ Earlier isotope substitution work provides additional support for these assignments.⁵⁵ The C=C stretching vibration is observed at 1530 cm⁻¹.⁵⁵ A C–H bending + C=C stretching combination band and a C–C stretching + C–F stretching combination band are monitored at 1440 and 1360 cm⁻¹, respectively.^{54,56} Likewise, the CF₃ vibrations and C–H bending modes are observed at 1250, 1230, and 1180 cm⁻¹, respectively.^{54,56}

Figure 2 shows the FTIR spectra from 4000 to 2400 cm⁻¹ after hfacH and Pt(hfac)₂ exposure on TiO₂ powders. These FTIR spectra display the higher frequency region of the spectra in Figure 1. The FTIR spectrum in Figure 2a shows a negligible absorbance change in the O–H stretching region following hfacH adsorption on TiO₂ at 200 °C. Because of the keto–enol equilibrium, hfacH could adsorb on TiO₂ in the keto or enol form. The lack of absorbance in the O–H stretching region argues that hfacH adsorbs on TiO₂ in the keto form. In addition, hfacH does not adsorb on the TiO₂ surface by

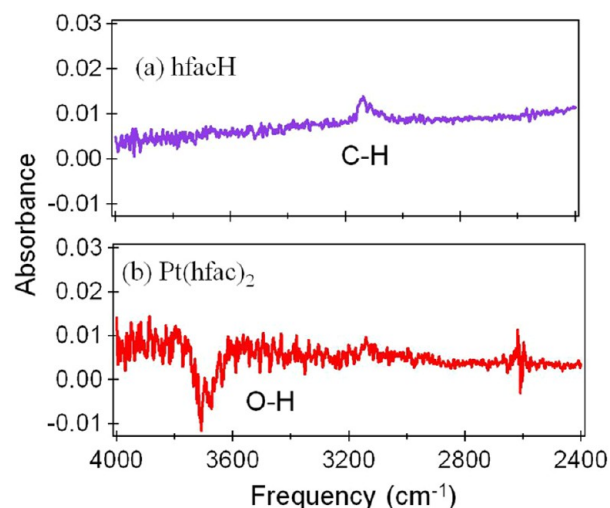


Figure 2. FTIR spectra in the O–H and C–H vibrational stretching region after adsorption of (a) hfacH and (b) Pt(hfac)₂ on TiO₂ powders at 200 °C. These spectra correspond to the same samples presented in Figure 1 and are referenced to the initial TiO₂ powders.

dissociative adsorption. Dissociative chemisorption would have added new O–H stretching vibrations on the TiO₂ surface. The addition of a C–H stretching vibration from the hfacH together with the absence of an O–H stretching vibration are consistent with the associative adsorption of hfacH in the keto form on TiO₂ powders.

The FTIR spectrum in Figure 2b displays a very small absorbance loss in the O–H stretching region following Pt(hfac)₂ adsorption on TiO₂ at 200 °C. This absorbance loss observed at ~3700 cm⁻¹ corresponds with the O–H stretching vibration of isolated hydroxyl groups on TiO₂.⁵⁷ This loss is consistent with a small fraction of the Pt(hfac)₂ molecules reacting with a few TiOH surface species. These absorbance changes argue that the dominant adsorption mechanism for Pt(hfac)₂ on TiO₂ powders is either associative adsorption or dissociative adsorption that does not release hydrogen to the TiO₂ surface. The presence of the infrared absorbance at ~2100 cm⁻¹ in Figure 1b corresponding with CO on Pt surfaces argues for some dissociative adsorption that would release Pt atoms and form Pt nanoparticles on the TiO₂ surface.^{48–51}

The FTIR spectra during the first two cycles of Pt ALD film growth on TiO₂ powders using Pt(hfac)₂ and formalin at 200 °C are shown in Figure 3. The Pt(hfac)₂ and formalin exposures yielded near saturation coverages. These FTIR spectra were all referenced to the initial TiO₂ powders. The FTIR spectrum in Figure 3a is very similar to the FTIR spectrum in Figure 1b. The absorbance for CO on Pt nanoparticles is again observed at ~2100 cm⁻¹. This peak indicates that Pt atoms are released from Pt(hfac)₂ and form Pt nanoparticles on the first Pt(hfac)₂ exposure on TiO₂. All the other infrared absorbances between 1800 and 1000 cm⁻¹ are nearly identical to the features observed and previously identified in Figure 1b.

Figure 3b shows that the subsequent formalin exposure increases the size of the infrared absorbance associated with CO on Pt nanoparticles. This increase is consistent with additional Pt atoms that increase the number and size of the Pt nanoparticles following formalin reduction of the adsorbed Pt(hfac)₂ surface species. The infrared absorbance is also

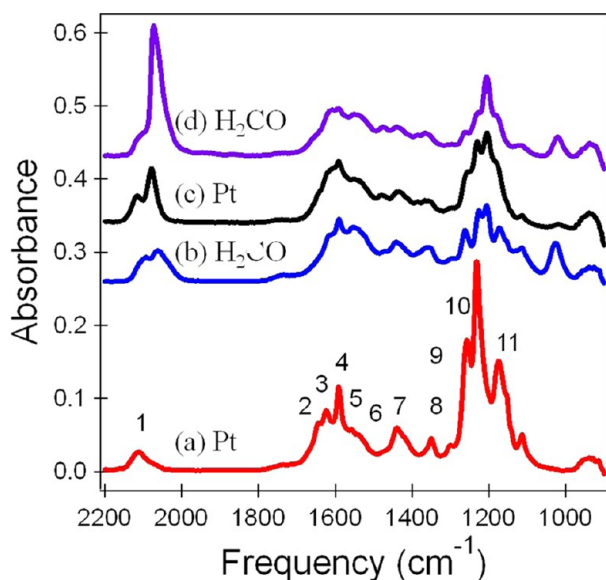


Figure 3. FTIR spectra after the first two cycles during Pt ALD on TiO_2 powders at $200\text{ }^\circ\text{C}$ with $\text{Pt}(\text{hfac})_2$ and formalin as the reactants. The spectra are referenced to the initial TiO_2 powders. (a) First $\text{Pt}(\text{hfac})_2$ exposure. (b) First formalin exposure. (c) Second $\text{Pt}(\text{hfac})_2$ exposure. (d) Second formalin exposure. The peak assignments are given in Table 1.

reduced significantly in the region of the CF_3 stretching vibrations. This reduction is consistent with the removal of hfac surface species.

The infrared absorbance is not reduced substantially in the carbonyl region between 1700 and 1500 cm^{-1} . Although CF_3 species are lost, there may be decomposition of hfac species that leaves carbonyl-containing reaction products on the TiO_2 surface. These species could include formate, carbonate, or ketenylidene species.⁵⁸ In addition, the formaldehyde (H_2CO) in the formalin exposure could also add carbonate and formate species.^{54,58}

Figure 3c shows that much smaller absorbance changes are observed after the second $\text{Pt}(\text{hfac})_2$ exposure during Pt ALD. The largest absorbance change is observed for CO on the Pt nanoparticles. This increase is consistent with the progressive growth of the number and size of the Pt nanoparticles. Only a small increase is observed for the absorbance of the CF_3 stretching vibrations at $\sim 1230\text{ cm}^{-1}$. The infrared absorbance in the carbonyl region shows very little change. However, the prominent feature observed at $\sim 1590\text{ cm}^{-1}$ for Pt associated with carbonyl features is missing in Figure 3c. The absence of this feature indicates that the $\text{Pt}(\text{hfac})_2$ adsorption products may bond differently to the formalin-exposed surface than the initial TiO_2 surface.

Figure 3d reveals that the subsequent formalin exposure leads to a much larger increase in the infrared absorbance for CO on the Pt nanoparticles. The formalin is able to reduce the $\text{Pt}(\text{hfac})_2$ surface species and liberate additional Pt atoms that can add to the existing Pt nanoparticles or form new Pt nanoparticles. There is also a slight reduction in the infrared absorbance for the CF_3 stretching vibrations that is consistent with the removal of some of the hfac surface species. Little change is observed in the carbonyl region between 1700 and 1500 cm^{-1} . This behavior again reveals that either hfac decomposition or the adsorption of formaldehyde or methanol is adding absorbance features in the carbonyl region.

Figure 4 explores the changes in the absorbance from 4000 to 900 cm^{-1} during the first Pt ALD cycle using FTIR

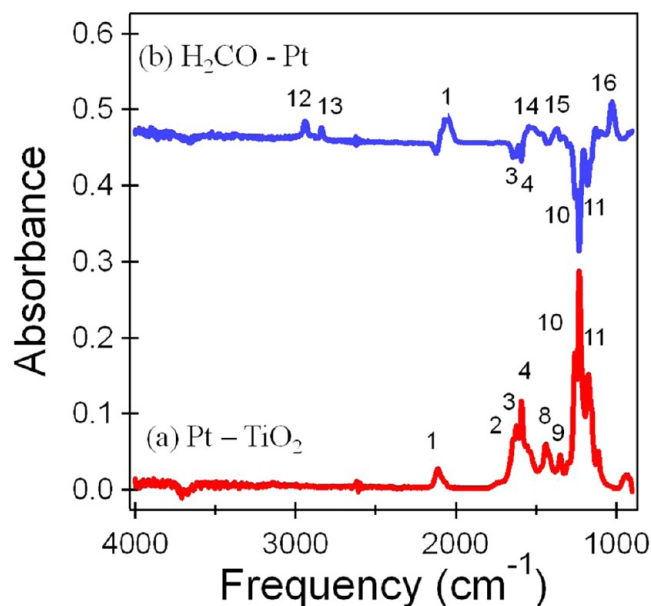


Figure 4. FTIR difference spectra during the first cycle during Pt ALD on TiO_2 powders at $200\text{ }^\circ\text{C}$ with $\text{Pt}(\text{hfac})_2$ and formalin as the reactants. (a) First $\text{Pt}(\text{hfac})_2$ exposure referenced to the initial TiO_2 powders. (b) First formalin exposure referenced to the initial $\text{Pt}(\text{hfac})_2$ exposure. The peak assignments are given in Table 1.

difference spectra that are referenced to the previous spectrum. These difference spectra are based on the spectra shown in Figure 3. Figure 4a shows the Pt– TiO_2 difference spectrum that references the FTIR spectrum after the $\text{Pt}(\text{hfac})_2$ exposure to the initial TiO_2 powders. Figure 4b shows the H_2CO –Pt difference spectrum that references the FTIR spectrum after the subsequent formalin exposure to the FTIR spectrum after the previous $\text{Pt}(\text{hfac})_2$ exposure. Additional vibrational assignments are given in Table 1 that identify the new absorbance features monitored after the formalin exposure.

The H_2CO –Pt difference spectrum in Figure 4b observes absorbance from C–H stretching vibrations after the formalin exposure that could be derived from formaldehyde or methanol.⁵⁹ The absorbance features associated with CO on Pt nanoparticles also display a distinctive shift to lower frequencies. This red shift is consistent with the reduction of the Pt atoms in the Pt nanoparticle by formalin.^{60–62} In contrast, a blue shift would be expected from the growth of larger Pt nanoparticles.^{61,63} There are also new features at 1370 and 1550 cm^{-1} that are consistent with the formation of formate and possibly carboxylate species on the surface.^{59,64,65} In addition, a new feature at $\sim 1026\text{ cm}^{-1}$ is observed that is assigned to a C–O stretching vibration.⁵⁹

Parts a and b of Figure 5 show the integrated absorbance in the CF_3 stretching and CH bending regions between 1100 and 1320 cm^{-1} versus time during $\text{Pt}(\text{hfac})_2$ and formalin exposures, respectively, during the second Pt ALD cycle at $200\text{ }^\circ\text{C}$ on TiO_2 powders. The exposures are performed using microdoses of $\text{Pt}(\text{hfac})_2$ or formalin. The microdoses are small exposures that are much less than the exposures required for saturation of the surface reaction. The surface chemistry is weakly self-limiting for the $\text{Pt}(\text{hfac})_2$ exposure. The surface chemistry is more completely self-limiting for the formalin

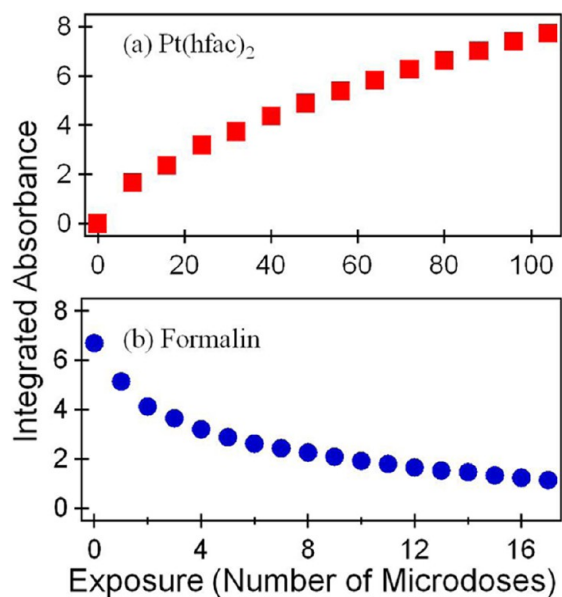


Figure 5. Integrated absorbance of the CF_3 stretching vibrations between 1100 and 1320 cm^{-1} during the adsorption of (a) $\text{Pt}(\text{hfac})_2$ and (b) formalin. These integrated absorbances were recorded during the second Pt ALD cycle on TiO_2 powders at $200\text{ }^\circ\text{C}$. The integrated absorbance was defined using modes 9–11 as assigned in Table 1.

exposure. The weak self-limiting behavior for $\text{Pt}(\text{hfac})_2$ may be associated with the large size of this reactant and the bulky nature of the hfac ligands. Rearrangements of adsorbed $\text{Pt}(\text{hfac})_2$ reactants may be required to open up space for additional $\text{Pt}(\text{hfac})_2$ reactants.

Figure 3d reveals that there is a large increase in the absorbance for the CO stretching vibrations on the Pt nanoparticles during the second formalin exposure. Figure 6 shows the evolution of the integrated absorbance for the CO stretching vibrations between 1990 and 2190 cm^{-1} during the second formalin exposure during Pt ALD. The second formalin exposure is the same series of microdoses as shown in Figure 5b. The integrated absorbance for the CO stretching vibrations increases dramatically during the early stages of the formalin

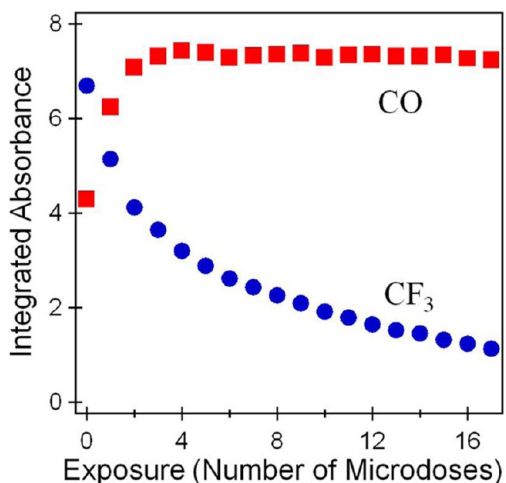


Figure 6. Integrated absorbance for the CO stretching vibration for CO on Pt nanoparticles and the CF_3 stretching vibration versus formalin exposure for a second formalin exposure during Pt ALD at $200\text{ }^\circ\text{C}$.

exposure. The integrated absorbance for the CO stretching vibrations is then relatively constant while the integrated absorbance of the CF_3 stretching vibrations is still reducing versus formalin exposure.

The results in Figure 6 suggest that Pt atoms are released quickly from $\text{Pt}(\text{hfac})_2$ adsorbed species during formalin reduction. These Pt atoms are presumably adding to existing Pt nanoparticles or forming new Pt nanoparticles. The formalin exposure then continues to remove hfac species on the TiO_2 substrate that contain CF_3 stretching vibrations. However, these hfac species on the TiO_2 substrate are not associated with additional Pt atoms.

Figure 7 shows the absorbance for the CO stretching vibrations on the Pt nanoparticles versus larger numbers of Pt

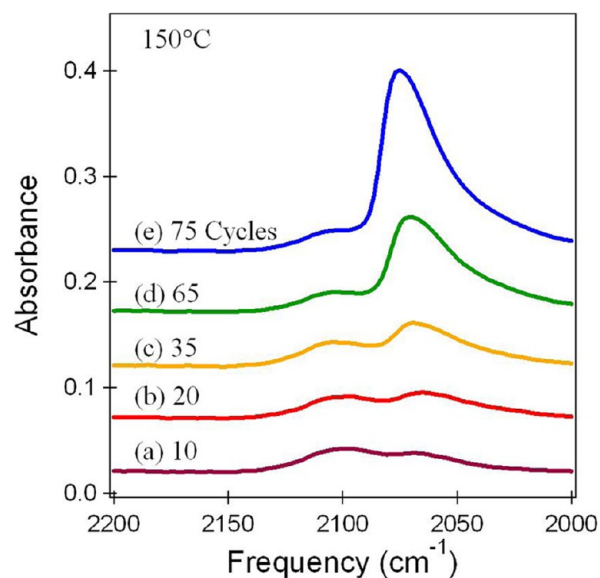


Figure 7. FTIR spectra in the CO vibrational stretching region after (a) 10, (b) 20, (c) 35, (d) 65, and (e) 75 Pt ALD cycles on TiO_2 powders at $150\text{ }^\circ\text{C}$.

ALD cycles at $150\text{ }^\circ\text{C}$. The temperature was reduced to $150\text{ }^\circ\text{C}$ to avoid desorption and decomposition of hfac ligands on the TiO_2 surface. Figure 7a reveals two broad peaks centered at ~ 2097 and $\sim 2065\text{ cm}^{-1}$ after 10 Pt ALD cycles. The peak at $\sim 2065\text{ cm}^{-1}$ then grows progressively after 20, 35, 65, and 75 Pt ALD cycles, as displayed in parts b, c, d, and e of Figure 7, respectively. For this set of Pt ALD cycles at $150\text{ }^\circ\text{C}$, TMA exposures were applied after 10, 20, 35, 45, and 70 Pt ALD cycles to remove the hfac species from the surface.¹² When spectra were recorded, they were collected prior to the TMA exposures.

The CO stretching vibration at $\sim 2065\text{ cm}^{-1}$ after 10 Pt ALD cycles shifts slightly to higher frequencies as this absorbance feature grows versus Pt ALD cycles. The CO stretching vibration is observed at $\sim 2070\text{ cm}^{-1}$ after 35 Pt ALD cycles and 2073 cm^{-1} after 75 Pt ALD cycles. This CO stretching frequency corresponds closely with the frequency of CO on on-top sites on stepped or defective $\text{Pt}(111)$ surfaces.^{66,67} This assignment is reasonable because small Pt nanoparticles cannot maintain large $\text{Pt}(111)$ terraces. In contrast, CO stretching vibrations on on-top sites on $\text{Pt}(111)$ single-crystal surfaces at full coverage are observed at $\sim 2100\text{ cm}^{-1}$.^{50,51}

The CO stretching vibration at $\sim 2097\text{ cm}^{-1}$ after 10 Pt ALD cycles shifts very slightly versus Pt ALD cycles. The CO

stretching vibration is observed at $\sim 2100\text{ cm}^{-1}$ after 65 Pt ALD cycles. Although this CO stretching vibration frequency is consistent with the CO stretching frequency on on-top sites on Pt(111) single-crystal surfaces at full coverage,^{50,51} small Pt nanoparticles could not have extensive Pt(111) surface area. Consequently, this CO stretching frequency is assigned to CO on more electropositive Pt clusters or surfaces.^{60–62} These more electropositive Pt clusters or surfaces may be associated with Pt that still retains some hfac coordination.

Figure 8 displays the TEM image of Pt nanoparticles on the TiO_2 powders after 150 cycles of Pt ALD at $200\text{ }^\circ\text{C}$. The

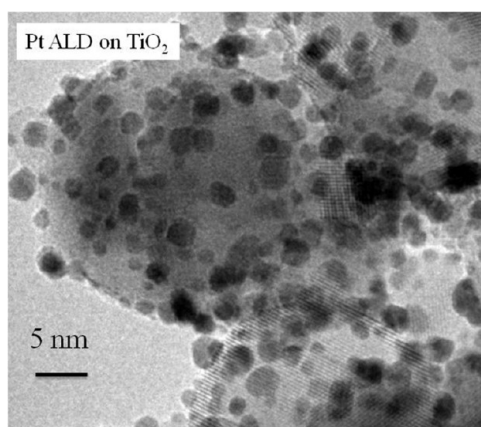


Figure 8. TEM image of Pt nanoparticles after 150 cycles of Pt ALD on TiO_2 powders at $200\text{ }^\circ\text{C}$ with $\text{Pt}(\text{hfac})_2$ and formalin as the reactants. The Pt nanoparticles have a diameter of $\sim 2\text{--}3\text{ nm}$ and the TiO_2 powder is crystalline.

$\text{Pt}(\text{hfac})_2$ and formalin exposures were sufficient to yield near saturation coverages after 20–30 Pt ALD cycles. The denser and darker Pt nanoparticles are on the lighter TiO_2 powder. Lattice fringes are observable in the individual grains of the TiO_2 powder. The Pt nanoparticles have a diameter of $\sim 2\text{--}3\text{ nm}$. Spherical Pt nanoparticle diameters of $\sim 2\text{ nm}$ have ~ 280 Pt atoms. Spherical Pt nanoparticle diameters of $\sim 3\text{ nm}$ have ~ 940 atoms. The coverage of the Pt nanoparticles is $\sim 6\text{--}7$ nanoparticles/100 nm^2 .

Figure 9 explores the FTIR spectra of $\text{Pt}(\text{hfac})_2$ and hfacH and the effect of hfacH preadsorption on the subsequent $\text{Pt}(\text{hfac})_2$ adsorption on TiO_2 powders at the lower temperature of $150\text{ }^\circ\text{C}$. The surface species are much more stable versus time at $150\text{ }^\circ\text{C}$. Figure 9a displays the FTIR spectrum after $\text{Pt}(\text{hfac})_2$ exposures sufficient to yield a near saturation $\text{Pt}(\text{hfac})_2$ coverage on TiO_2 powders at $150\text{ }^\circ\text{C}$. This spectrum is very similar to the spectra in Figure 1b and Figure 3a recorded after $\text{Pt}(\text{hfac})_2$ adsorption at $200\text{ }^\circ\text{C}$. Figure 9b displays the FTIR spectrum after hfacH exposures sufficient to yield a near saturation hfacH coverage on TiO_2 powders at $150\text{ }^\circ\text{C}$. This spectrum is very similar to the spectrum in Figure 1a recorded after hfacH adsorption at $200\text{ }^\circ\text{C}$.

Figure 9c shows the FTIR spectrum after exposing hfacH to the TiO_2 powders and obtaining a near saturation hfacH exposure prior to a subsequent exposure of $\text{Pt}(\text{hfac})_2$. The $\text{Pt}(\text{hfac})_2$ exposure would have been sufficient to yield a near saturation coverage on clean TiO_2 powders. Figure 9d displays the FTIR difference spectrum defined by the FTIR spectrum in Figure 9c referenced to the FTIR spectrum in Figure 9b.

A comparison between the FTIR spectra in parts d and a of Figure 9 shows that the preadsorbed hfacH dramatically

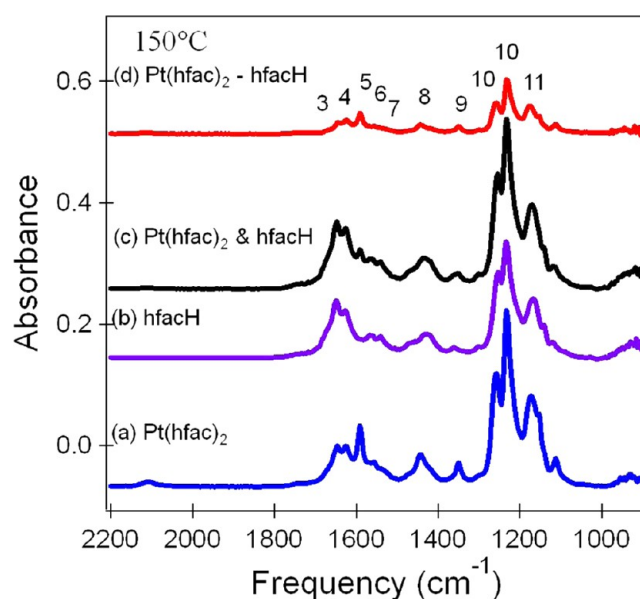


Figure 9. FTIR spectra after adsorption on TiO_2 powders at $150\text{ }^\circ\text{C}$. (a) Adsorption of $\text{Pt}(\text{hfac})_2$. (b) Adsorption of hfacH. (c) Adsorption of $\text{Pt}(\text{hfac})_2$ after preadsorption of hfacH. (d) $\text{Pt}(\text{hfac})_2$ –hfacH difference spectra showing absorbance gain after adsorbing $\text{Pt}(\text{hfac})_2$ on surface covered with hfacH.

reduces the adsorption of $\text{Pt}(\text{hfac})_2$ on the TiO_2 powders. The absorbances in the CF_3 and carbonyl stretching vibration regions in Figure 9d are much less than the corresponding absorbances in Figure 9a. The preadsorbed hfacH has blocked the available adsorption sites for $\text{Pt}(\text{hfac})_2$. This site-blocking by hfacH may also serve to reduce the coverage of Pt nanoparticles on the TiO_2 powders.

Figure 10 displays TEM images of Pt nanoparticles grown using 150 Pt ALD cycles with $\text{Pt}(\text{hfac})_2$ and formalin at $200\text{ }^\circ\text{C}$. The $\text{Pt}(\text{hfac})_2$ and formalin exposures were sufficient to yield near saturation coverages after 20–30 Pt ALD cycles. Figure 10a shows the Pt nanoparticles resulting from 150 Pt ALD cycles on initial TiO_2 powders. Figure 10b shows the Pt nanoparticles resulting from 150 Pt ALD cycles on TiO_2 powders that had been initially exposed to a near saturation exposure of hfacH. The preadsorbed hfacH on the TiO_2 powders dramatically reduces the coverage of Pt nanoparticles.

The Pt nanoparticle coverage in Figure 10a is $\sim 6\text{--}7$ nanoparticles/100 nm^2 without the preadsorbed hfacH. The Pt nanoparticle coverage in Figure 10b is $\sim 1\text{--}3$ nanoparticles/100 nm^2 with the preadsorbed hfacH. The Pt nanoparticle diameter is also reduced by the preadsorbed hfacH on the TiO_2 powders. The Pt nanoparticle diameter is $\sim 2\text{--}3\text{ nm}$ without the preadsorbed hfacH in Figure 10a. The Pt nanoparticle diameter is $\sim 1.5\text{ nm}$ with the preadsorbed hfacH in Figure 10b. The lower Pt nanoparticle coverages and smaller Pt nanoparticle diameters are consistent with fewer Pt atoms deposited by $\text{Pt}(\text{hfac})_2$ on the TiO_2 surface with preadsorbed hfacH.

Preadsorbed hfacH can dramatically reduce the subsequent adsorption of $\text{Pt}(\text{hfac})_2$ on TiO_2 surfaces. The hfac ligands from $\text{Pt}(\text{hfac})_2$ should also be able to block sites and prevent the adsorption of additional $\text{Pt}(\text{hfac})_2$ reactants. Similar behavior was observed for Pd ALD using $\text{Pd}(\text{hfac})_2$ and formalin as the reactants.¹³ Earlier studies of Pd ALD using $\text{Pd}(\text{hfac})_2$ and formalin demonstrated that trimethylaluminum (TMA) could remove the $\text{Pt}(\text{hfac})_2$ adsorption products and facilitate a more

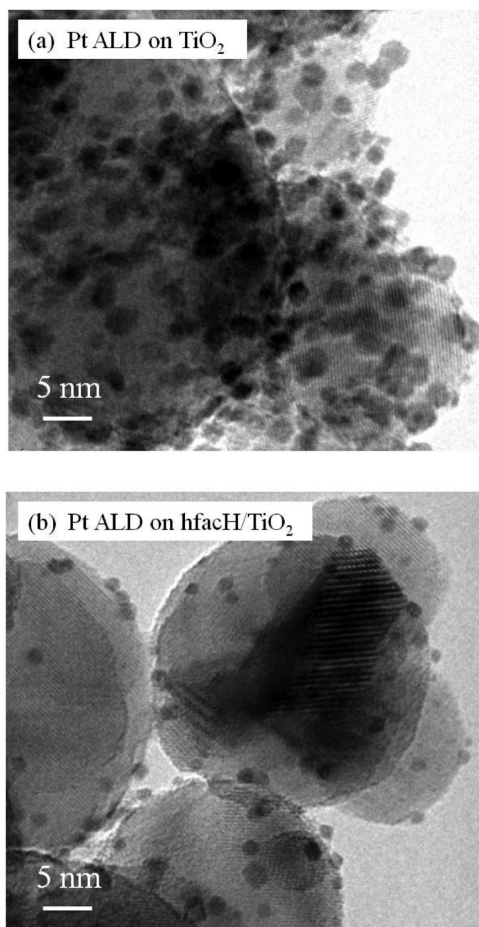


Figure 10. TEM images comparing Pt nanoparticles grown using (a) Pt ALD on TiO_2 powders and (b) Pt ALD on TiO_2 powders initially exposed to hfach. The Pt nanoparticles were grown using 150 Pt ALD cycles with $\text{Pt}(\text{hfac})_2$ and formalin at 200°C . The preadsorbed hfach on the TiO_2 powders dramatically reduces the coverage of Pt nanoparticles.

rapid nucleation of Pt ALD.¹² TMA should also be able to remove the $\text{Pt}(\text{hfac})_2$ adsorption products during Pt ALD using $\text{Pt}(\text{hfac})_2$ and formalin as the reactants.

The ability of hfach to restrict $\text{Pt}(\text{hfac})_2$ adsorption and lower the Pt nanoparticle coverage on the TiO_2 surface may be dependent on the coverage of the hfach reaction products. The hfach reaction products can be adjusted by allowing the adsorbed hfach to either desorb or decompose following hfach adsorption. Figure 11a shows the FTIR spectrum of hfach on TiO_2 powders after a hfach exposure at 200°C that was sufficient to yield a near saturation coverage. Parts b, c, and d of Figure 11 then show the FTIR difference spectra versus times of 5, 42, and 118 min, respectively. The difference spectra reveal that the hfach adsorption products are progressively lost from the TiO_2 surface versus time at 200°C .

The loss of the hfach adsorption products from TiO_2 is very temperature dependent. Figure 12 shows the integrated absorbance versus time at temperatures of 175, 200, 225, and 250°C after hfach exposures that were sufficient to yield near saturation coverages. The integrated absorbance was defined using the carbonyl stretching vibrations between 1500 and 1745 cm^{-1} as defined by modes 2–6 in Table 1. The loss of the hfach adsorption products is much more rapid at higher temperatures. The higher temperatures also led to a loss of the

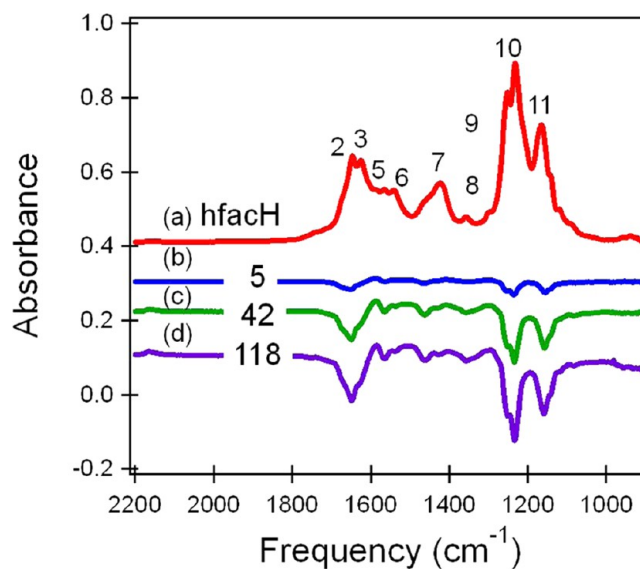


Figure 11. (a) FTIR spectrum recorded after hfach exposure on TiO_2 powders at 200°C . Difference spectra recorded versus time after (b) 5 min, (c) 42 min, and (d) 118 min. The difference spectra are referenced to the FTIR spectrum in part a. The difference spectra reveal the desorption and decomposition of the adsorbed hfach species versus time.

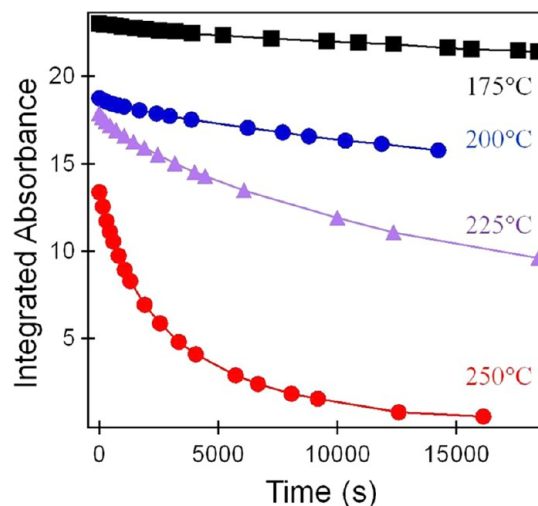


Figure 12. Integrated absorbance between 1500 and 1745 cm^{-1} versus time at 175, 200, 225, and 250°C after the adsorption of hfach on TiO_2 powders at the given temperature. The integrated absorbance was defined using modes 2–6 as assigned in Table 1.

integrated absorbance prior to the recording of the first FTIR spectrum.

An estimate of the activation energy for the loss of hfach adsorption products can be obtained using the initial slopes of the integrated absorbance versus time plots and assuming a first-order loss mechanism. The loss mechanism may include both hfach desorption and hfach decomposition.⁵⁸ On the basis of an Arrhenius analysis of the initial slope results versus temperature, an activation energy of $96 \pm 9\text{ kJ/mol}$ was obtained from the results in Figure 12. This activation energy on the TiO_2 surface is less than the activation energy of 165 kJ/mol that was obtained for hfach second-order desorption from Al_2O_3 ALD surfaces.¹³

TiO₂ powders provided a convenient substrate for the FTIR studies of Pt ALD and Pt nanoparticle formation because the TiO₂ powders are insulators and are not conducting. Consequently, the TiO₂ powders did not display background infrared absorption. Pt nanoparticles on other oxide substrates, such as tungsten oxide, are relevant for fuel cells.^{34–37} Tungsten oxide can also be electrically conductive. Electrical conductivity is needed for electron transport in PEM fuel cells. However, the electrical conductivity of WO_x nanorods precludes their use for FTIR studies because of background infrared absorption according to the Drude–Zener theory.^{68,69}

To compare Pt ALD on TiO₂ powders and WO_x nanorods, Pt nanoparticles were grown using 150 cycles of Pt ALD with Pt(hfac)₂ and formalin as the reactants at 200 °C. The Pt(hfac)₂ and formalin exposures were sufficient to yield near saturation coverages on TiO₂ powders after 20–30 Pt ALD cycles. Parts a and b of Figure 13 show the TEM images for Pt

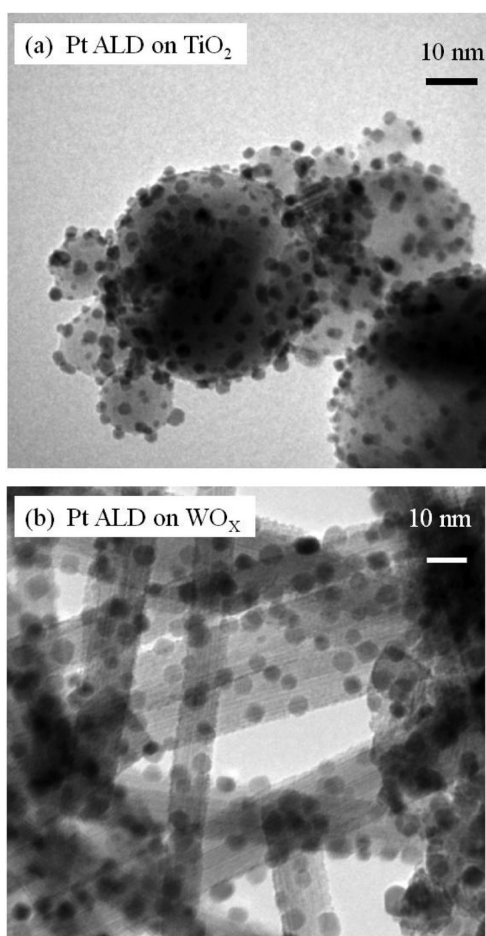


Figure 13. TEM images comparing Pt nanoparticles grown using (a) Pt ALD on TiO₂ powders and (b) Pt ALD on WO_x nanorods. The Pt nanoparticles were grown using 150 Pt ALD cycles with Pt(hfac)₂ and formalin at 200 °C.

ALD on TiO₂ powders and WO_x nanorods, respectively. The average Pt nanoparticle diameters are ~2–3 and ~4–5 nm on the TiO₂ and WO_x surfaces, respectively. The average Pt nanoparticle coverages are ~6–7 and ~2–3 nanoparticles/100 nm² on the TiO₂ and WO_x surfaces, respectively. These contrasting Pt nanoparticle coverages and sizes indicate that the growth mechanisms are slightly different on the two substrates.

Figure 14 displays a higher resolution TEM image of Pt nanoparticles on a WO_x nanorod after 170 cycles of Pt ALD at

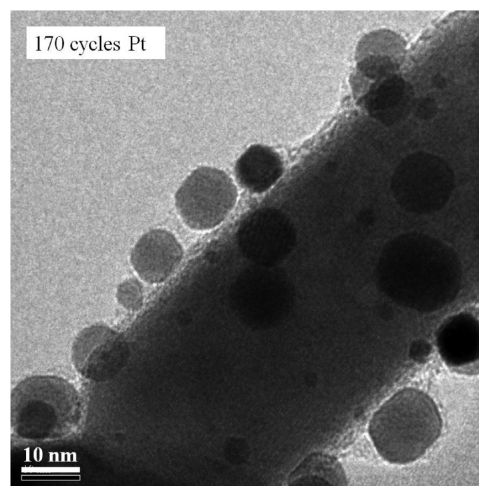


Figure 14. TEM image of Pt nanoparticles on a WO_x nanorod. The Pt nanoparticles were grown using 170 Pt ALD cycles with Pt(hfac)₂ and formalin at 200 °C. To facilitate the Pt ALD nucleation, the first 20 Pt ALD cycles included a TMA exposure after the formalin exposure.

200 °C. The Pt(hfac)₂ and formalin exposures were sufficient to yield near saturation coverages on TiO₂ powders after 20–30 Pt ALD cycles. The first 20 Pt ALD cycles were performed with a TMA exposure after the formalin exposure to remove the Pt(hfac)₂ and formalin adsorption products.¹² This TEM image illustrates the highly spherical nature of the Pt nanoparticles. Spherical shapes are consistent with the high surface energy of Pt, which fosters the formation of spherical Pt particles to minimize the surface area to lower the surface energy.

Pt nanoparticles were also grown on WO_x nanorods at 200 °C using various numbers of Pt ALD cycles with Pt(hfac)₂ and formalin as the reactants. The Pt(hfac)₂ and formalin exposures were sufficient to yield near saturation coverages on TiO₂ powders after 20–30 Pt ALD cycles. Figure 15 shows TEM images of Pt nanoparticles after 130, 140, and 150 Pt ALD cycles. The Pt nanoparticle diameter increased with the number of Pt ALD cycle. The Pt nanoparticle diameters were ~2.0, ~2.2, and ~4.5 nm after 130, 140, and 150 Pt ALD cycles, respectively. The corresponding Pt nanoparticle coverages were ~1, ~2–3, and ~2–3 nanoparticles/100 nm² after 130, 140, and 150 Pt ALD cycles, respectively. The growth of Pt nanoparticles versus Pt ALD cycles has also been observed for Pt ALD on TiO₂,^{17,19} carbon nanotube/graphene,¹⁶ SiO₂,²⁹ Al₂O₃,¹⁸ and SrTiO₃ substrates.²⁴

The growth of the Pt nanoparticle diameters observed in Figure 15 is not linear with the number of Pt ALD cycles. This nonlinearity may be related to the nucleation of Pt ALD on WO_x nanorods. A certain number of Pt ALD cycles may be required before reaching the threshold for efficient Pt ALD growth. A similar behavior was observed for Pd ALD on the Al₂O₃ ALD surface using Pd(hfac)₂ and formalin as the reactants.¹¹ This delayed nucleation was explained earlier in terms of the time required to remove the hfac adsorption products from the surface that block Pd(hfac)₂ adsorption sites and restrict Pd ALD growth.^{12,13}

Because of site-blocking by the hfac ligands, the Pt nanoparticles grown using Pt(hfac)₂ and formalin require

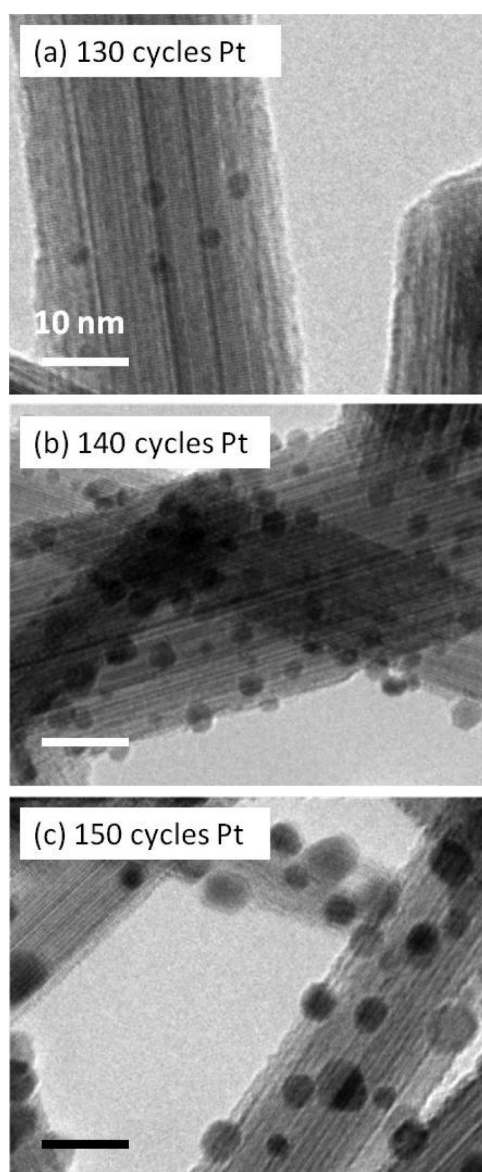


Figure 15. TEM images of Pt nanoparticles on WO_x nanorods grown using (a) 130 Pt ALD cycles, (b) 140 Pt ALD cycles, and (c) 150 Pt ALD cycles with $\text{Pt}(\text{hfac})_2$ and formalin at 200 °C.

many more cycles to obtain comparable diameters than Pt nanoparticles grown using other Pt ALD surface chemistries. Using MeCpPtMe_3 and O_2 as the reactants on TiO_2 , Pt nanoparticle diameters of ~ 1 and $\sim 2\text{--}3$ nm were obtained after one and 20 Pt ALD cycles, respectively.¹⁹ Using MeCpPtMe_3 and ozone as the reactants on TiO_2 , Pt nanoparticle diameters of ~ 1.5 and ~ 2.3 nm were obtained after one and five Pt ALD cycles, respectively.¹⁷ Similar results were observed on SiO_2 ,²⁹ SrTiO_3 ,²⁴ and Al_2O_3 substrates¹⁸ using MeCpPtMe_3 and O_2 .

The hfac ligands block sites on oxide surfaces and can dramatically increase the number of Pt ALD cycles required for nucleation and growth. However, the site-blocking properties of hfacH can also be used to control the coverage of Pt nanoparticles. The disadvantage of requiring more Pt ALD cycles can become an advantage when site-blocking can help control the Pt nanoparticle coverage. We note that hfacH could be used together with other surface chemistries for Pt ALD or

other metal ALD to control the reactant adsorption and tune the metal nanoparticle coverage.

Finally, XPS studies were performed to determine the purity of the Pt deposited by Pt ALD using $\text{Pt}(\text{hfac})_2$ and formalin. Samples were grown using ~ 400 cycles of Pt ALD on TiO_2 powders at 200 °C. The $\text{Pt}(\text{hfac})_2$ and formalin exposures were sufficient to yield near saturation coverages on TiO_2 powders after 20–30 Pt ALD cycles. These samples were then analyzed using XPS. After removing the adventitious carbon with Ar sputtering, XPS analysis was consistent with 95 atom % Pt on the TiO_2 powders.

4. CONCLUSIONS

$\text{Pt}(\text{hfac})_2$ and formalin were used as the reactants to grow Pt nanoparticles on titanium oxide and tungsten oxide at 200 °C using Pt ALD. The Pt ALD surface chemistry during the initial Pt ALD cycles on titanium oxide was studied using in situ FTIR spectroscopy. The Pt nanoparticles were analyzed on both titanium oxide and tungsten oxide using ex situ TEM.

The FTIR spectrum of $\text{Pt}(\text{hfac})_2$ on TiO_2 was very similar to the FTIR spectrum of hfacH on TiO_2 . The lack of changes in the O–H stretching region after hfacH adsorption and small loss of absorbance in the O–H stretching region after $\text{Pt}(\text{hfac})_2$ adsorption argued that both hfacH and $\text{Pt}(\text{hfac})_2$ adsorb primarily via associative adsorption on TiO_2 . Any dissociative adsorption occurred without the transfer of hydrogen to the TiO_2 surface.

The repetitive application of the $\text{Pt}(\text{hfac})_2$ and formalin exposures led to changes in the absorbance for the CF_3 stretching vibrations and only small changes in the absorbance for the carbonyl species. The results suggested that formalin was able to remove many of the hfac surface species. However, the decomposition of hfac species or adsorption of carbonyl-containing species during the formalin exposure prevented the observation of an absorbance loss in the carbonyl region of the FTIR spectrum. The FTIR spectra also showed that the surface chemical reactions versus $\text{Pt}(\text{hfac})_2$ and formalin exposures were weakly self-limiting.

An infrared feature at $\sim 2100\text{ cm}^{-1}$ was monitored in the FTIR spectrum that was consistent with CO on Pt nanoparticles. The absorbance for the CO stretching vibration on the Pt nanoparticles was observed to increase rapidly during the initial stages of the formalin exposure. This behavior suggested that the $\text{Pt}(\text{hfac})$ species were reduced and liberated Pt atoms prior to the removal of the other hfac surface species. The absorbance of the CO stretching frequency at 2070 cm^{-1} grew progressively with Pt ALD cycles and was consistent with CO adsorbed on on-top sites on stepped or defective Pt(111) surfaces.

The FTIR spectra also revealed that adsorbed hfacH blocked the subsequent adsorption of $\text{Pt}(\text{hfac})_2$ on TiO_2 . The coverage of the Pt nanoparticles could be reduced by preadsorbing hfacH on the TiO_2 prior to $\text{Pt}(\text{hfac})_2$ adsorption. The Pt nanoparticle coverage was reduced from $\sim 6\text{--}7$ to $\sim 1\text{--}3$ nanoparticles/100 nm^2 with preadsorbed hfacH. The corresponding Pt nanoparticle diameter was reduced from $\sim 2\text{--}3$ to ~ 1.5 nm with preadsorbed hfacH.

Pt ALD on WO_x powders at 200 °C led to the growth of Pt nanoparticles that were fairly similar to the Pt nanoparticles after Pt ALD on TiO_2 powders. The size of the Pt nanoparticles on WO_x powders increased with the number of Pt ALD cycles. The Pt nanoparticles grown using $\text{Pt}(\text{hfac})_2$ and formalin required many more cycles to obtain comparable diameters

than Pt nanoparticles grown using other Pt ALD surface chemistries. The larger number of required Pt ALD cycles is attributed to the site-blocking effects of hfac species.

AUTHOR INFORMATION

Corresponding Author

*E-mail: steven.george@colorado.edu.

Notes

The authors declare no competing financial interest.

ACKNOWLEDGMENTS

This work is dedicated to Dr. Anne C. Dillon, who was a former student and collaborator. Her early passing took away a colleague with deep insight and infectious enthusiasm. This work was funded by the DOE under the EERE Fuel Cell Technology Program. We thank Dr. Andrew Cavanagh for X-ray photoelectron spectroscopy (XPS) sample analysis. We also appreciate useful conversations on Pt ALD with Dr. Layton Baker, who is now at the Jet Propulsion Laboratory.

REFERENCES

- (1) Ellinger, C.; Stierle, A.; Robinson, I. K.; Nefedov, A.; Dosch, H. Atmospheric Pressure Oxidation of Pt(111). *J. Phys.-Condens. Mater.* **2008**, *20*, 184013.
- (2) Gasteiger, H. A.; Kocha, S. S.; Sompalli, B.; Wagner, F. T. Activity Benchmarks and Requirements for Pt, Pt-Alloy, and Non-Pt Oxygen Reduction Catalysts for PEMFCs. *Appl. Catal., B* **2005**, *56*, 9–35.
- (3) George, S. M. Atomic Layer Deposition: An Overview. *Chem. Rev.* **2010**, *110*, 111–131.
- (4) Aaltonen, T.; Ritala, M.; Sajavaara, T.; Keinonen, J. Atomic Layer Deposition of Platinum Thin Films. *Chem. Mater.* **2003**, *15*, 1924–1928.
- (5) Aaltonen, T.; Rahtu, A.; Ritala, M.; Leskela, M. Reaction Mechanism Studies on Atomic Layer Deposition of Ruthenium and Platinum. *Electrochem. Solid State Lett.* **2003**, *6*, C130–C130.
- (6) Kessels, W. M. M.; Knoops, H. C. M.; Dielissen, S. A. F.; Mackus, A. J. M.; van de Sanden, M. C. M. Surface Reactions during Atomic Layer Deposition of Pt Derived from Gas Phase Infrared Spectroscopy. *Appl. Phys. Lett.* **2009**, *95*, 013114.
- (7) Baker, L.; Cavanagh, A. S.; Seghete, D.; George, S. M.; Mackus, A. J. M.; Kessels, W. M. M.; Liu, Z. Y.; Wagner, F. T. Nucleation and Growth of Pt Atomic Layer Deposition on Al₂O₃ Substrates Using (Methylcyclopentadienyl)trimethyl Platinum and O₂ Plasma. *J. Appl. Phys.* **2011**, *109*, 084333.
- (8) Knoops, H. C. M.; Mackus, A. J. M.; Donders, M. E.; van de Sanden, M. C. M.; Notten, P. H. L.; Kessels, W. M. M. Remote Plasma ALD of Platinum and Platinum Oxide Films. *Electrochem. Solid State Lett.* **2009**, *12*, G34–G36.
- (9) Hamalainen, J.; Munnik, F.; Ritala, M.; Leskela, M. Atomic Layer Deposition of Platinum Oxide and Metallic Platinum Thin Films from Pt(acac)₂ and Ozone. *Chem. Mater.* **2008**, *20*, 6840–6846.
- (10) Baker, L.; Cavanagh, A. S.; Yin, J.; George, S. M.; Kongkanand, A.; Wagner, F. T. Growth of Continuous and Ultrathin Platinum Films on Tungsten Adhesion Layers Using Atomic Layer Deposition Techniques. *Appl. Phys. Lett.* **2012**, *101*, 111601.
- (11) Elam, J. W.; Zinovev, A.; Han, C. Y.; Wang, H. H.; Welp, U.; Hryn, J. N.; Pellin, M. J. Atomic Layer Deposition of Palladium Films on Al₂O₃ Surfaces. *Thin Solid Films* **2006**, *515*, 1664–1673.
- (12) Goldstein, D. N.; George, S. M. Enhancing the Nucleation of Palladium Atomic Layer Deposition on Al₂O₃ Using Trimethylaluminum To Prevent Surface Poisoning by Reaction Products. *Appl. Phys. Lett.* **2009**, *95*, 143106.
- (13) Goldstein, D. N.; George, S. M. Surface Poisoning in the Nucleation and Growth of Palladium Atomic Layer Deposition with Pd(hfac)₂ and Formalin. *Thin Solid Films* **2011**, *519*, 5339–5347.
- (14) King, J. S.; Wittstock, A.; Biener, J.; Kucheyev, S. O.; Wang, Y. M.; Baumann, T. F.; Giri, S. K.; Hamza, A. V.; Baeumer, M.; Bent, S. F. Ultralow Loading Pt Nanocatalysts Prepared by Atomic Layer Deposition on Carbon Aerogels. *Nano Lett.* **2008**, *8*, 2405–2409.
- (15) Liu, C.; Wang, C. C.; Kei, C. C.; Hsueh, Y. C.; Perng, T. P. Atomic Layer Deposition of Platinum Nanoparticles on Carbon Nanotubes for Application in Proton-Exchange Membrane Fuel Cells. *Small* **2009**, *5*, 1535–1538.
- (16) Hsieh, C. T.; Liu, Y. Y.; Tzou, D. Y.; Chen, W. Y. Atomic Layer Deposition of Platinum Nanocatalysts onto Three-Dimensional Carbon Nanotube/Graphene Hybrid. *J. Phys. Chem. C* **2012**, *116*, 26735–26743.
- (17) Goulas, A.; van Ommen, J. R. Atomic Layer Deposition of Platinum Clusters on Titania Nanoparticles at Atmospheric Pressure. *J. Mater. Chem. A* **2013**, *1*, 4647–4650.
- (18) Setthapun, W.; Williams, W. D.; Kim, S. M.; Feng, H.; Elam, J. W.; Rabuffetti, F. A.; Poepelmeier, K. R.; Stair, P. C.; Stach, E. A.; Ribeiro, F. H.; Miller, J. T.; Marshall, C. L. Genesis and Evolution of Surface Species during Pt Atomic Layer Deposition on Oxide Supports Characterized by In Situ XAFS Analysis and Water–Gas Shift Reaction. *J. Phys. Chem. C* **2010**, *114*, 9758–9771.
- (19) Zhou, Y.; King, D. M.; Liang, X.; Li, J.; Weimer, A. W. Optimal Preparation of Pt/TiO₂ Photocatalysts Using Atomic Layer Deposition. *Appl. Catal., B* **2010**, *101*, 54–60.
- (20) Lei, Y.; Liu, B.; Lu, J. L.; Lobo-Lapidus, R. J.; Wu, T. P.; Feng, H.; Xia, X. X.; Mane, A. U.; Libera, J. A.; Greeley, J. P.; Miller, J. T.; Elam, J. W. Synthesis of Pt–Pd Core–Shell Nanostructures by Atomic Layer Deposition: Application in Propane Oxidative Dehydrogenation to Propylene. *Chem. Mater.* **2012**, *24*, 3525–3533.
- (21) Christensen, S. T.; Elam, J. W.; Lee, B.; Feng, Z.; Bedzyk, M. J.; Hersam, M. C. Nanoscale Structure and Morphology of Atomic Layer Deposition Platinum on SrTiO₃(001). *Chem. Mater.* **2009**, *21*, 516–521.
- (22) Christensen, S. T.; Elam, J. W.; Rabuffetti, F. A.; Ma, Q.; Weigand, S. J.; Lee, B.; Seifert, S.; Stair, P. C.; Poepelmeier, K. R.; Hersam, M. C.; Bedzyk, M. J. Controlled Growth of Platinum Nanoparticles on Strontium Titanate Nanocubes by Atomic Layer Deposition. *Small* **2009**, *5*, 750–757.
- (23) Enterkin, J. A.; Poepelmeier, K. R.; Marks, L. D. Oriented Catalytic Platinum Nanoparticles on High Surface Area Strontium Titanate Nanocuboids. *Nano Lett.* **2011**, *11*, 993–997.
- (24) Enterkin, J. A.; Setthapun, W.; Elam, J. W.; Christensen, S. T.; Rabuffetti, F. A.; Marks, L. D.; Stair, P. C.; Poepelmeier, K. R.; Marshall, C. L. Propane Oxidation over Pt/SrTiO₃ Nanocuboids. *ACS Catal.* **2011**, *1*, 629–635.
- (25) Lin, Y. H.; Hsueh, Y. C.; Wang, C. C.; Wu, J. M.; Perng, T. P.; Shih, H. C. Enhancing the Photon-Sensing Properties of ZnO Nanowires by Atomic Layer Deposition of Platinum. *Electrochem. Solid St. Lett.* **2010**, *13*, K93–K95.
- (26) Hsu, I. J.; Hansgen, D. A.; McCandless, B. E.; Willis, B. G.; Chen, J. G. Atomic Layer Deposition of Pt on Tungsten Monocarbide (WC) for the Oxygen Reduction Reaction. *J. Phys. Chem. C* **2011**, *115*, 3709–3715.
- (27) Novak, S.; Lee, B.; Yang, X. Y.; Misra, V. Platinum Nanoparticles Grown by Atomic Layer Deposition for Charge Storage Memory Applications. *J. Electrochem. Soc.* **2010**, *157*, H589–H592.
- (28) Weber, M. J.; Mackus, A. J. M.; Verheijen, M. A.; van der Marel, C.; Kessels, W. M. M. Supported Core/Shell Bimetallic Nanoparticles Synthesis by Atomic Layer Deposition. *Chem. Mater.* **2012**, *24*, 2973–2977.
- (29) Li, J. H.; Liang, X. H.; King, D. M.; Jiang, Y. B.; Weimer, A. W. Highly Dispersed Pt Nanoparticle Catalyst Prepared by Atomic Layer Deposition. *Appl. Catal., B* **2010**, *97*, 220–226.
- (30) Shim, J. H.; Jiang, X.; Bent, S. F.; Prinz, F. B. Catalysts with Pt Surface Coating by Atomic Layer Deposition for Solid Oxide Fuel Cells. *J. Electrochem. Soc.* **2010**, *157*, B793–B797.
- (31) Elliott, S. D. Mechanism, Products, and Growth Rate of Atomic Layer Deposition of Noble Metals. *Langmuir* **2010**, *26*, 9179–9182.

- (32) Vitos, L.; Ruban, A. V.; Skriver, H. L.; Kollar, J. The Surface Energy of Metals. *Surf. Sci.* **1998**, *411*, 186–202.
- (33) Campbell, C. T. Ultrathin Metal Films and Particles on Oxide Surfaces: Structural, Electronic and Chemisorptive Properties. *Surf. Sci. Rep.* **1997**, *27*, 1–111.
- (34) Cui, X. Z.; Guo, L. M.; Cui, F. M.; He, Q. J.; Shi, J. L. Electrocatalytic Activity and CO Tolerance Properties of Mesoporous Pt/WO₃ Composite as an Anode Catalyst for PEMFCs. *J. Phys. Chem. C* **2009**, *113*, 4134–4138.
- (35) Ganesan, R.; Lee, J. S. An Electrocatalyst for Methanol Oxidation Based on Tungsten Trioxide Microspheres and Platinum. *J. Power Sources* **2006**, *157*, 217–221.
- (36) Lewera, A.; Timperman, L.; Roguska, A.; Alonso-Vante, N. Metal-Support Interactions between Nanosized Pt and Metal Oxides (WO₃ and TiO₂) Studied Using X-ray Photoelectron Spectroscopy. *J. Phys. Chem. C* **2011**, *115*, 20153–20159.
- (37) Shim, J.; Lee, C. R.; Lee, H. K.; Lee, J. S.; Cairns, E. J. Electrochemical Characteristics of Pt–WO₃/C and Pt–TiO₂/C Electrocatalysts in a Polymer Electrolyte Fuel Cell. *J. Power Sources* **2001**, *102*, 172–177.
- (38) Feng, H.; Elam, J. W.; Libera, J. A.; Setthapun, W.; Stair, P. C. Palladium Catalysts Synthesized by Atomic Layer Deposition for Methanol Decomposition. *Chem. Mater.* **2010**, *22*, 3133–3142.
- (39) Feng, H.; Libera, J. A.; Stair, P. C.; Miller, J. T.; Elam, J. W. Subnanometer Palladium Particles Synthesized by Atomic Layer Deposition. *ACS Catal.* **2011**, *1*, 665–673.
- (40) Liang, X. H.; Lyon, L. B.; Jiang, Y. B.; Weimer, A. W. Scalable Synthesis of Palladium Nanoparticle Catalysts by Atomic Layer Deposition. *J. Nanoparticle Res.* **2012**, *14*, 943.
- (41) Lu, J.; Stair, P. C. Nano/Subnanometer Pd Nanoparticles on Oxide Supports Synthesized by AB-Type and Low-Temperature ABC-Type Atomic Layer Deposition: Growth and Morphology. *Langmuir* **2010**, *26*, 16486–16495.
- (42) Goldstein, D. N.; McCormick, J. A.; George, S. M. Al₂O₃ Atomic Layer Deposition with Trimethylaluminum and Ozone Studied by In Situ Transmission FTIR Spectroscopy and Quadrupole Mass Spectrometry. *J. Phys. Chem. C* **2008**, *112*, 19530–19539.
- (43) Ballinger, T. H.; Smith, R. S.; Colson, S. D.; Yates, J. T. Thermal-Decomposition of 1,1,1-Trichloroethane and 1,1-Dichloroethane over High Surface-Area Alumina. *Langmuir* **1992**, *8*, 2473–2478.
- (44) Ferguson, J. D.; Weimer, A. W.; George, S. M. Atomic Layer Deposition of Ultrathin and Conformal Al₂O₃ Films on BN Particles. *Thin Solid Films* **2000**, *371*, 95–104.
- (45) Mahan, A. H.; Parilla, P. A.; Jones, K. M.; Dillon, A. C. Hot-Wire Chemical Vapor Deposition of Crystalline Tungsten Oxide Nanoparticles at High Density. *Chem. Phys. Lett.* **2005**, *413*, 88–94.
- (46) Crane, E. L.; You, Y.; Nuzzo, R. G.; Girolami, G. S. Mechanistic Studies of CVD Metallization Processes: Reactions of Rhodium and Platinum Beta-Diketonate Complexes On Copper Surfaces. *J. Am. Chem. Soc.* **2000**, *122*, 3422–3435.
- (47) Lin, W.; Wiegand, B. C.; Nuzzo, R. G.; Girolami, G. S. Mechanistic Studies of Palladium Thin Film Growth from Palladium(II) Beta-Diketonates. 1. Spectroscopic Studies of the Reactions of Bis(hexafluoroacetylacetonato)palladium(II) on Copper Surfaces. *J. Am. Chem. Soc.* **1996**, *118*, 5977–5987.
- (48) Anderson, J. A. Infrared Study of the Oxidation of Carbon Monoxide over Pt/Al₂O₃. *J. Chem. Soc. Faraday Trans.* **1992**, *88*, 1197–1201.
- (49) Brandt, R. K.; Hughes, M. R.; Bourget, L. P.; Truszkowska, K.; Greenler, R. G. The Interpretation of CO Adsorbed on Pt/SiO₂ of Two Different Particle-Size Distributions. *Surf. Sci.* **1993**, *286*, 15–25.
- (50) Crossley, A.; King, D. A. Infrared Spectra for CO Isotopes Chemisorbed on Pt(111): Evidence for Strong Adsorbate Coupling Interactions. *Surf. Sci.* **1977**, *68*, 528–538.
- (51) Hayden, B. E.; Bradshaw, A. M. The Adsorption of CO on Pt(111) Studied by Infrared Reflection–Absorption Spectroscopy. *Surf. Sci.* **1983**, *125*, 787–802.
- (52) Hadjiivanov, K. FTIR Study of CO and NH₃ Co-Adsorption on TiO₂ (Rutile). *Appl. Surf. Sci.* **1998**, *135*, 331–338.
- (53) Hadjiivanov, K.; Lamotte, J.; Lavalley, J. C. FTIR Study of Low-Temperature CO Adsorption on Pure and Ammonia-Precovered TiO₂ (Anatase). *Langmuir* **1997**, *13*, 3374–3381.
- (54) Farkas, J.; Hampden-Smith, M. J.; Kotas, T. T. FTIR Studies of the Adsorption/Desorption Behavior of Copper Chemical Vapor Deposition Precursors on Silica. 1. Bis(1,1,1,5,5,5-Hexafluoroacetylacetonato)Copper(II). *J. Phys. Chem.* **1994**, *98*, 6753–6762.
- (55) Pinchas, S.; Silver, B. L.; Laulicht, I. Infrared Absorption Spectra of the ¹⁸O Labeled Acetylacetonates of Cr(III) and Mn(III). *J. Chem. Phys.* **1967**, *46*, 1506–1510.
- (56) Morris, M. L.; Moshier, R. W.; Sievers, R. E. Infrared Spectra of Metal Chelate Compounds of Hexafluoroacetylacetonate. *Notes Inorg. Chem.* **1963**, 411–412.
- (57) Van Thiel, M.; Becker, E. D.; Pimentel, G. C. Infrared Studies of Hydrogen Bonding of Water by the Matrix Isolation Technique. *J. Chem. Phys.* **1957**, *27*, 486–490.
- (58) Girolami, G. S.; Jeffries, P. M.; Dubois, L. H. Mechanistic Studies of Copper Thin-Film Growth from Cu(I) and Cu(II) Beta-Diketonates. *J. Am. Chem. Soc.* **1993**, *115*, 1015–1024.
- (59) Kecskés, T.; Raskó, J.; Kiss, J. FTIR and Mass Spectrometric Studies on the Interaction of Formaldehyde with TiO₂ Supported Pt and Au Catalysts. *Appl. Catal. A-Gen.* **2004**, *273*, 55–62.
- (60) Gruene, P.; Fielicke, A.; Meijer, G.; Rayner, D. M. The Adsorption of CO on Group 10 (Ni, Pd, Pt) Transition-Metal Clusters. *Phys. Chem. Chem. Phys.* **2008**, *10*, 6144–6149.
- (61) Park, S.; Wasileski, S. A.; Weaver, M. J. Electrochemical Infrared Characterization of Carbon-Supported Platinum Nanoparticles: A Benchmark Structural Comparison with Single-Crystal Electrodes and High-Nuclearity Carbonyl Clusters. *J. Phys. Chem. B* **2001**, *105*, 9719–9725.
- (62) Wu, X.; Zhang, L.; Weng, D.; Liu, S.; Si, Z.; Fan, J. Total Oxidation of Propane on Pt/WO_x/Al₂O₃ Catalysts by Formation of Metastable Pt⁺ Species Interacted with WO_x Clusters. *J. Hazard. Mater.* **2012**, *225*–226, 146–154.
- (63) Baranova, E. A.; Bock, C.; Ilin, D.; Wang, D.; MacDougall, B. Infrared Spectroscopy on Size-Controlled Synthesized Pt-Based Nano-Catalysts. *Surf. Sci.* **2006**, *600*, 3502–3511.
- (64) Busca, G.; Lorenzelli, V. Infrared Spectroscopic Identification of Species Arising from Reactive Adsorption of Carbon Oxides on Metal Oxide Surfaces. *Mater. Chem.* **1982**, *7*, 89–126.
- (65) Hayden, B. E.; King, A.; Newton, M. A. Fourier Transform Reflection–Absorption IR Spectroscopy Study of Formate Adsorption on TiO₂(110). *J. Phys. Chem. B* **1999**, *103*, 203–208.
- (66) Klünker, C.; Balden, M.; Lehwald, S.; Daum, W. CO Stretching Vibrations on Pt (111) and Pt (110) Studied by Sum-Frequency Generation. *Surf. Sci.* **1996**, *360*, 104–111.
- (67) Xu, A.; Yates, J. T., Jr. Terrace Width Effect on Adsorbate Vibrations: A Comparison of Pt(335) and Pt(112) for Chemisorption of CO. *Surf. Sci.* **1995**, *327*, 193–201.
- (68) Baraton, M. I.; Merhari, L. Determination of the Gas Sensing Potentiality of Nanosized Powders by FTIR Spectrometry. *Scripta Mater.* **2001**, *44*, 1643–1648.
- (69) Kahn, A. H. Theory of the Infrared Absorption of Carriers in Germanium and Silicon. *Phys. Rev.* **1955**, *97*, 1647–1652.